
Air–Sea Interaction and Horizontal Circulation in the Red Sea

Amy S. Bower and J. Thomas Farrar

Abstract

This chapter discusses the horizontal circulation of the Red Sea and the surface meteorology that drives it, and recent satellite and in situ measurements from the region are used to illustrate properties of the Red Sea circulation and the atmospheric forcing. The surface winds over the Red Sea have rich spatial structure, with variations in speed and direction on both synoptic and seasonal timescales. Wintertime mountain-gap wind jets drive large heat losses and evaporation at some locations, with as much as 9 cm of evaporation in a week. The near-surface currents in the Red Sea exhibit similarly rich variability, with an energetic and complex flow field dominated by persistent, quasi-stationary eddies, and convoluted boundary currents. At least one quasi-stationary eddy pair is driven largely by winds blowing through a gap in the mountains (Tokar Gap), but numerical simulations suggest that much of the eddy field is driven by the interaction of the buoyancy-driven flow with topography. Recent measurements suggest that Gulf of Aden Intermediate Water (GAIW) penetrates further northward into the Red Sea than previously reported.

Air–Sea Interaction

Regional Meteorology

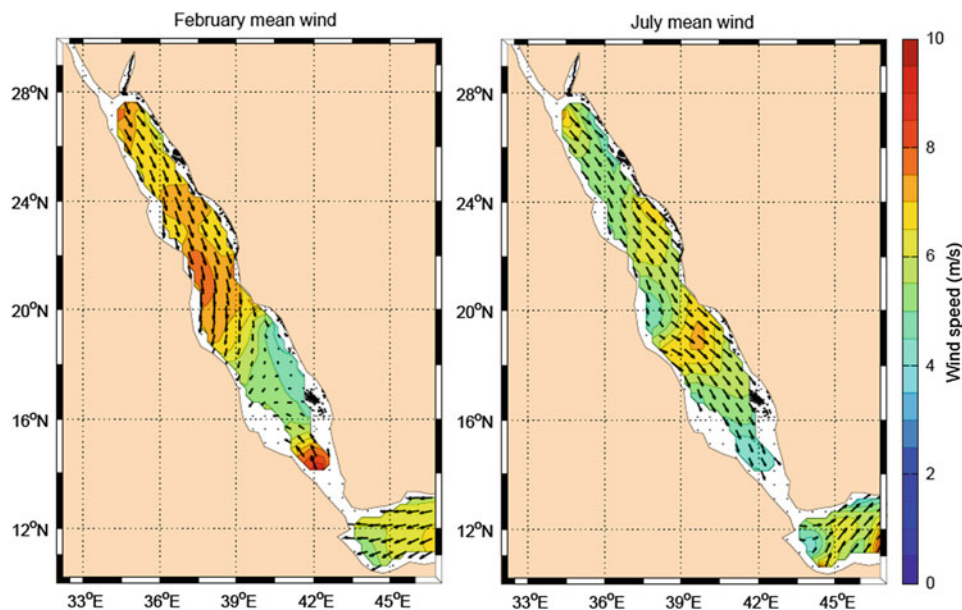
The water circulation of the Red Sea is driven by the exchange of momentum, heat, and freshwater with the overlying atmosphere. The continental landmasses surrounding the Red Sea exert a profound influence on the regional meteorology and air–sea fluxes and hence on the Red Sea circulation. The relatively narrow basin (maximum width 355 km) is located between Africa and the Arabian subcontinent, and the landmasses surrounding the Red Sea can be classified as arid land, desert, or semi-desert (Naval Oceanography Command Detachment 1993). The dry air flowing over the Red Sea from these arid landmasses helps to make it a site of intense evaporation, with the basin-averaged evaporation estimated to be about 2 m/yr (Sofianos et al. 2002).

The coastal mountain chains bordering the Red Sea along both the African and Arabian coasts also exert significant influence on the regional meteorology, primarily by constraining the mean, large-scale surface winds to flow along the axis of the basin (Fig. 1; Patzert 1974). The seasonal winds blow toward the southeast all year in the northern part of the basin (north of 19–20°N), but in the southern part of the basin, the winds reverse from northwesterly in summer to southeasterly in winter under the influence of the two distinct phases of the Arabian monsoon (Fig. 1; Pedgley 1974; Patzert 1974; Clifford et al. 1997; Sofianos and Johns 2003; Jiang et al. 2009).

This seasonally reversing wind is associated with substantial spatial variations in mean wind speeds, with speed variations of about a factor of two between different parts of the basin (Fig. 1; using the 10-year climatology of QuikSCAT scatterometer winds of Risien and Chelton 2008). The monsoonal circulation and associated wind reversal in the southern part of the basin also contribute to distinct regional differences in the annual cycle of wind speed; the south-central part of the basin (16–20°N) experiences the strongest winds in summer, but the rest of the basin, especially the

A.S. Bower (✉) · J.T. Farrar
Department of Physical Oceanography, Woods Hole
Oceanographic Institution, Woods Hole, MA, USA
e-mail: abower@whoi.edu

Fig. 1 Climatological monthly mean surface winds for February (*left*) and July (*right*), at the two extremes of the annual cycle of surface winds in the Red Sea. The colored contours indicate wind speed, and the vectors depict the direction and relative speed. The climatological means are based on data from the QuikSCAT satellite scatterometer from September 1999 to October 2009 (Risien and Chelton 2008)



northern and southern ends of the Red Sea, experiences the strongest winds in winter (Fig. 1). During winter, the surface winds converge in the south-central part of the basin (roughly 16–20°N), leading to relatively weak wind speeds (<4 m/s) in this region. Some of the converging air flows out of the basin through the Tokar Gap and other gaps in the coastal mountain ranges (e.g., Jiang et al. 2009). During summer, the prevailing winds are more spatially uniform, both in speed and direction.

Gaps in the coastal mountain chains also affect the surface wind field on smaller scales, with intense mountain-gap wind jets blowing across the Red Sea from Africa during summer (e.g., Hickey and Goudie 2007) and from the Arabian subcontinent during winter (Jiang et al. 2009). Figure 2, from Jiang et al. (2009), illustrates the structure of the surface wind field during the summertime and wintertime wind jet events in simulations carried out using the Weather Research and Forecasting (WRF) model. The effect of these strong transient wind events on the currents of the Red Sea is not well understood, but field measurements from one site in the central Red Sea suggest that the effect of these wind jets on the air–sea exchange of heat and freshwater is significant, as is discussed in the next subsection.

Heat and Freshwater Fluxes

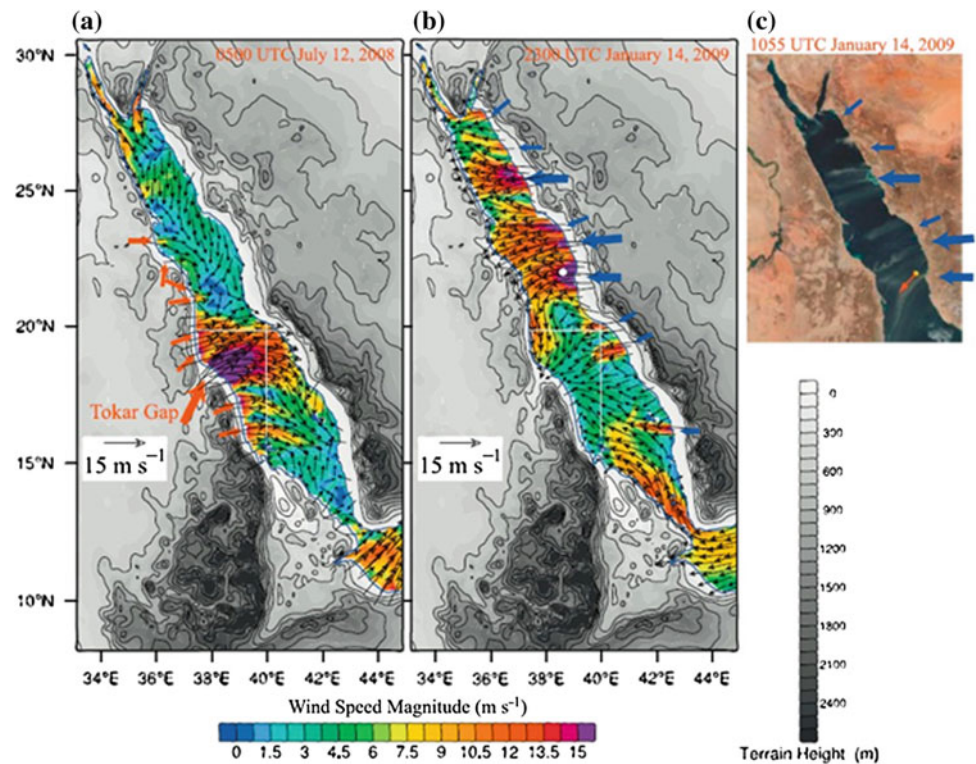
The mean circulation of the Red Sea is believed to be driven primarily by surface buoyancy fluxes associated with the mean loss of heat and freshwater to the atmosphere, both of which act to make the surface waters of the Red Sea denser (Sofianos and Johns 2003). The freshwater budget of the Red Sea is dominated by evaporation, which tends to make the Red Sea saltier, and by the flow of water through the

Strait of Bab-al-Mandab, where relatively freshwater flows in at the surface from the Gulf of Aden and salty Red Sea overflow water spills from the Red Sea to the Gulf of Aden at depth (e.g., Murray and Johns 1997).

The best available constraints on the areal-average surface fluxes of heat and freshwater in the Red Sea come from observations of currents and water properties at the Strait of Bab-al-Mandab, used together with the fact that the heat and freshwater transport through this strait must be balanced by the air–sea fluxes of heat and freshwater over the Red Sea (e.g., Tragou et al. 1999; Sofianos et al. 2002). Sofianos et al. (2002) estimated the areal-average heat and freshwater loss to the atmosphere to be $11 \pm 5 \text{ W/m}^2$ and $2.06 \pm 0.22 \text{ m/yr}$. More direct estimates of the basin-average surface heat and freshwater fluxes in the Red Sea from meteorological measurements and bulk flux formulas have proven problematic because of measurement and sampling errors in the meteorological observations available from voluntary observing ships and in the bulk formulas for solar and infrared radiative fluxes (e.g., Tragou et al. 1999).

Accurate and direct estimates of the air–sea fluxes of heat and freshwater at a site in the central Red Sea (22°9'N, 38°30'W; location indicated in Fig. 2) comes from detailed measurements of surface meteorology and solar and infrared radiation from a heavily instrumented air–sea interaction mooring deployed by the Woods Hole Oceanographic Institution (WHOI) in collaboration with the King Abdullah University of Science and Technology (KAUST). The surface buoy carried instruments to measure wind, humidity, temperature, precipitation, air pressure, sea surface temperature, solar (or “shortwave”) radiation, and infrared (or “longwave”) radiation (Farrar et al. 2009), which have been used together with the COARE bulk flux algorithm (Fairall

Fig. 2 Surface winds (10 m height) in high-resolution WRF model simulations for July 12, 2008 (a) and January 14, 2009 (b), (c) visible imagery taken by the MODIS instrument on NASA's Aqua satellite on January 14, 2009, showing dust plumes being carried over the Red Sea from the Arabian Peninsula. The location of the air–sea interaction buoy is shown by a *small circle* in panels (b) and (c). From Jiang et al. (2009)



et al. 2003) to estimate the air–sea heat fluxes of heat, momentum, and freshwater (Fig. 3). The mean evaporation rate at the site was about 1.98 m/yr, and the mean net heat flux was about -14 W/m^2 .

These measurements at one location do not provide any direct constraints for the basin-average fluxes discussed in the previous paragraph, but they can provide some insight

into the nature of the errors in available surface flux products. For example, the 2 years of buoy measurements are compared to two surface heat flux climatologies in Fig. 3. A flux climatology derived from the database of weather observations from ships (Josey et al. 1999) overestimates the net heat flux at the site by about 60 W/m^2 , having a mean value that is about $+44 \text{ W/m}^2$ (whereas the

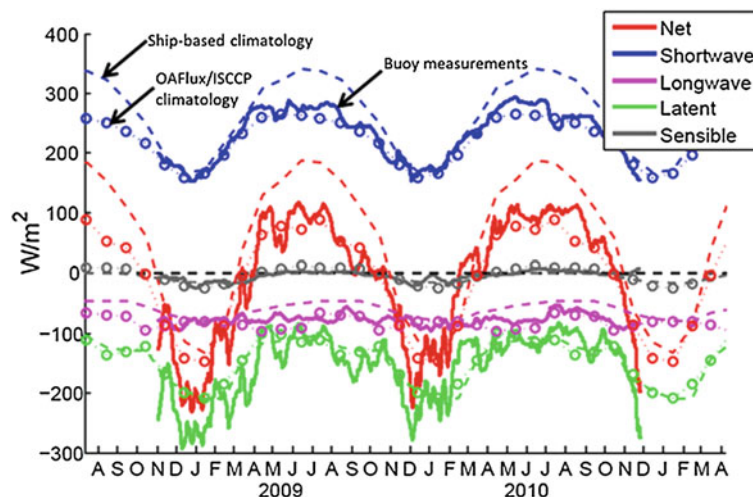


Fig. 3 Air–sea heat flux components (*solid lines*) estimated from measurements of surface radiation, and meteorology on an air–sea interaction buoy maintained in the central Red Sea by WHOI and KAUST (Farrar et al. 2009). The *dashed lines* show climatological values estimated from weather observations reported by volunteer observing ships (Josey et al. 1999), and the *dotted lines* with large

circles show climatological values estimated from a combination of satellite data, atmospheric reanalysis products, and other data (Yu and Weller 2007). The estimates of shortwave (or solar) and longwave (or infrared) radiation from the ship-based climatology are based on bulk formulas rather than direct measurements, and these quantities account for most of the disagreement with the measured values.

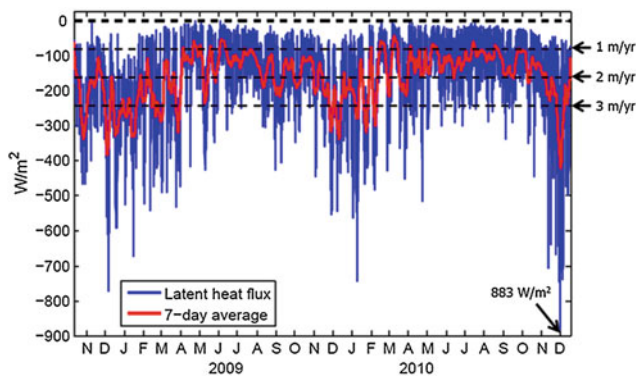


Fig. 4 Latent heat flux at the buoy site (22.15°N, 38.5°E). The blue line shows 1 h average latent heat fluxes, which reach values exceeding 500 W/m² during wintertime mountain-gap wind events. Latent heat flux is proportional to the evaporation rate, and the black dashed lines indicate the corresponding evaporation rates

net heat flux measured at the buoy was -14 W/m^2). A flux climatology computed from an objective analysis of satellite data, atmospheric reanalysis products, and other data (OA-Flux; Yu and Weller 2007) agrees with the 2-year-average net heat flux at the buoy to within about 2 W/m^2 . We refer below to differences between the flux climatologies and the buoy records as “errors,” but we note that some differences between the climatological surface fluxes and the fluxes over a particular 2-year time period should be expected. About half of the error ($+30 \text{ W/m}^2$) in the ship-based climatology comes from the estimate of the solar radiation, which was estimated in the flux product from a bulk formula that depends on the fraction of the sky obscured by clouds. An additional $+17 \text{ W/m}^2$ comes from the infrared radiation (where the plus sign means too little infrared radiation is coming from the sky), which is similarly dependent on cloud cover fraction. (Most of the remaining disagreement, 12 W/m^2 , comes from the latent heat flux). It seems likely that the large errors in solar and infrared radiation result from neglect of regional aerosol effects from airborne dust (e.g., as in Fig. 2c). ” can be changed to “ISCCP.”” →The OAFlux product uses surface solar and infrared radiation products estimated from the International Satellite Cloud Climatology Project (ISCCP) data and a radiative transfer model that explicitly accounts for regional and seasonal variations in atmospheric aerosols (Zhang et al. 2004). The ISCCP-derived radiative flux product has much smaller errors (-8.5 W/m^2 in solar and -5.3 W/m^2 in infrared) than the radiative fluxes estimated from ship observations and bulk formulas. These biases in radiative fluxes compensate for overestimation of the latent and sensible heat fluxes (by $+15.2$ and $+1.0 \text{ W/m}^2$, respectively).

The 2-year record of latent heat flux shows a strong seasonal cycle in evaporation, with weekly average evaporation rates varying from about 1 m/yr in the summer months

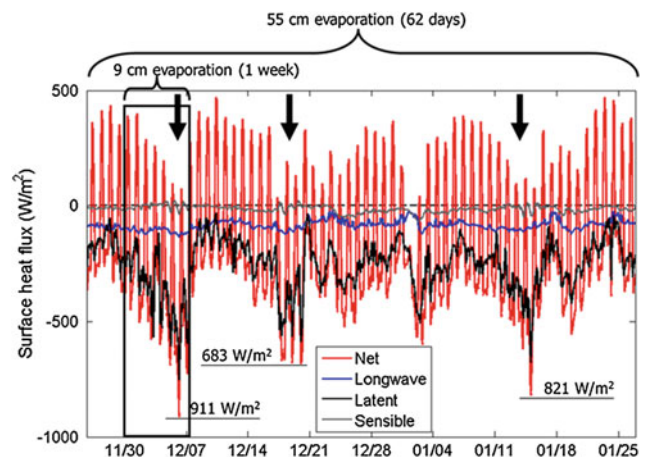


Fig. 5 Heat flux components at the buoy site during a period spanning three mountain-gap wind events in the winter of 2008–2009. The times of occurrence of the three wind events are indicated by heavy black arrows. During the first event in early December, there was about 9 cm of evaporation, about 4.5 % of the annual average evaporation at the site

to about 3 m/yr in the winter months (Fig. 4). There are also many large evaporation events during the wintertime, with hourly average evaporative heat losses frequently exceeding 500 W/m^2 (Fig. 4). These evaporation events are associated with the occurrence of the wintertime mountain-gap wind events discussed by Jiang et al. (2009). The buoy data indicate that these events bring relatively cool ($\sim 20^\circ\text{C}$), dry (specific humidity of $\sim 7 \text{ g/kg}$) air from the Arabian subcontinent. For the three mountain-gap wind events occurring in December 2008 and January 2009 (Jiang et al. 2009), the peak hourly average heat losses estimated from the buoy measurements were 911, 683, and 821 W/m^2 (Fig. 5). During a week-long period surrounding the strongest of those events (Fig. 5), about 9 cm of water was evaporated from the sea surface—this is about 4.5 % of the annual mean evaporation at the site (1 week is about 1.9 % of a year). About 55 cm of evaporation, or 28 % of the annual mean, took place over the longer, 62 day period shown in Fig. 5; 62 days are only about 17 % of a year. The wintertime wind jet events thus contribute substantially to the annual mean evaporation and heat loss at the buoy site.

Much of the northern half of the Red Sea is affected by these wind jets (Fig. 2), so it seems likely that these wintertime wind jets provide an important contribution to the basin-average evaporation and heat loss. Papadopoulos et al. (2013) analyzed a daily surface flux product and found that the most intense wintertime heat loss in the northern part of the Red Sea (north of 25°N) tends to occur when the large-scale atmospheric conditions favor westward winds over the northern Red Sea. This occurs when there is a region of atmospheric high pressure that extends westward from the Siberian high to the Arabian subcontinent and the

Mediterranean Sea (Papadopoulos et al. 2013). These are the same conditions that are associated with the occurrence of the intense wintertime wind jet events (Jiang et al. 2009 and their Figure S1). The Papadopoulos et al. (2013) analysis identified a fairly close correspondence between the pattern of mean wintertime heat loss and the standard deviation of the heat flux, which suggests that atmospheric synoptic variability makes important contributions to the wintertime heat loss. However, the flux product analyzed by Papadopoulos et al. (2013) is too coarse to spatially resolve the individual wind jets, and individual examination of the most extreme heat loss events in the far northern part of the basin showed a range of synoptic conditions, including some that were conducive to westward wind jets and some that were not, so further study of the conditions driving the largest wintertime heat loss is still needed.

Horizontal Circulation

Our understanding of how wind stress and surface fluxes of heat and freshwater impact the three-dimensional structure of the Red Sea circulation and its variability is still rudimentary. This is due largely to the limited number of sustained in situ observations of currents and water properties. Satellite-borne sensors that have now measured sea surface temperature, color, and elevation for multiple years have been helpful in identifying some Red Sea circulation surface features and estimating average trends in sea surface temperature (e.g., Acker et al. 2008; Raitso et al. 2011, 2013), but remote sensing measurements have one or more limitations, including low spatial resolution, no subsurface information, lack of coverage near coastlines, no direct current information, and lost data due to clouds and dust in the atmosphere.

The most comprehensive studies to date of the basin-scale Red Sea circulation and its variability have been mainly those based on analyses of output from ocean general circulation models (OGCMs), which are usually forced with relatively low-resolution ($\geq 1^\circ$) global wind and buoyancy flux products from atmospheric re-analyses (Clifford et al. 1997; Eshel and Naik 1997; Sofianos and Johns 2003; Biton et al. 2008; Yao et al. 2014a, b). With the exception of Bab-al-Mandab, where an 18-month time series of the exchange flow between the Red Sea and the Gulf of Aden provides a benchmark for testing OGCM performance (Murray and Johns 1997; Sofianos et al. 2002), most data sets on currents and water properties are spatially and/or temporally compromised, allowing for only limited verification of model output (Clifford et al. 1997; Yao et al. 2014a, b). Furthermore, since the physical environment is of fundamental importance to other oceanographic processes, including primary production, biogeochemical cycles, coral reef ecosystem dynamics, and interaction between the coral reefs

and the open Red Sea, the overall oceanographic knowledge base in the Red Sea is low compared to some other similarly sized ocean basins. Here, we review earlier observational and numerical model studies of the horizontal circulation in the Red Sea and present some new results collected during two major hydrographic expeditions to the Red Sea in 2010 and 2011.

Eddies and Gyres

Many studies of the basin-scale circulation in the Red Sea have focused on the two-dimensional (latitude depth) thermohaline-driven overturning circulation, which includes a two-way (winter) or three-way (summer) exchange flow through Bab-al-Mandab (e.g., Phillips 1966; Tragou and Garrett 1997; Murray and Johns 1997; see also Sofianos and Johns, this volume, for a complete discussion). The overturning is driven by a net evaporation on the order of 2 m/yr over the Red Sea (Ahmad and Albarakati, this volume). However, regional observations and numerical simulations have revealed that the overturning circulation, with its annual mean transport on the order of 0.4 Sv, is embedded in a complex, three-dimensional pattern of currents consisting of large, energetic, quasi-stationary eddies (also called gyres or sub-gyres by some authors), and narrow boundary currents, with transports that are an order of magnitude larger than the overturning circulation (e.g., Morcos 1970; Morcos and Soliman 1972; Maillard 1971; Sofianos and Johns 2003). Both clockwise (anticyclonic) and anti-clockwise (cyclonic) eddies appear in observations and model output, often with diameters similar to the width of the basin (about 100–200 km—much larger than the 40 km Rossby radius of deformation; Zhai and Bower 2013) and with the strongest currents in the upper several hundred meters.

In the first basin-scale study of these eddies, Quadfasel and Baudner (1993) used CTD and repeated XBT sections made along and across the central axis during 1983–1987 to show that the Red Sea is often filled with a north–south stack of eddies with surface geostrophic azimuthal speeds (relative to 400 dbar) of up to 0.6 m/s and circular transports of 1–3 Sv. This pattern of stacked eddies was recently confirmed with an along-axis transect of velocity measured using a vessel-mounted acoustic Doppler current profiler (ADCP) by Sofianos and Johns (2007). With their repeated transects, Quadfasel and Baudner (1993) found that anticyclonic eddies are more prevalent than cyclonic eddies and that the eddies appear to be quasi-stationary, trapped in four subregions of the Red Sea (in the latitude bands 17° – 19° N, 19° – 21.5° N, 21.5° – 24° N and 24° – 27° N). They argued that the eddies are generated when along-axis currents resulting from positive and negative wind stress curl on either side of the prevailing along-axis wind jet are deflected across the basin

by coastal capes and promontories, forming closed circulation cells in the several sub-basins of the Red Sea.

On the other hand, Clifford et al. (1997) emphasized the importance of the *cross-basin* component of the wind field, arguing that this introduces larger wind stress curl and subsequently more eddies in the Red Sea. They ran two numerical experiments with a high-resolution (6-km grid spacing) primitive equation OGCM, one forced with low-resolution (40-km grid spacing) wind fields and another forced with higher-resolution (grid spacing about the same as the OGCM) wind fields that were corrected to more accurately follow the local orography. In both cases, more eddies appeared when there was a cross-basin component to the wind field. However, in the case with orographically steered winds, there was more wind stress curl and consequently more and stronger eddies in the model velocity fields. Jiang et al. (2009) recently confirmed the importance of mountain gaps on both sides of the Red Sea in funneling wind into intense cross-basin jets using the WRF model and a high-resolution regional atmospheric model.

The impact of one particular cross-basin wind jet, the Tokar Jet, on Red Sea eddy generation was recently studied by Zhai and Bower (2013). This eastward wind jet originates in the Tokar Gap on the Sudanese coast at about 19°N during most summers and can reach amplitudes of 20–25 m/s (Pedgley 1974; Jiang et al. 2009). Zhai and Bower used time series of scatterometer wind fields and altimeter-derived sea level anomalies (SLA) to identify a strong dipolar eddy that often appears in summer centered near 19°N with a horizontal scale of ~140 km, shortly after the onset of the wind jet. They showed that the positive and negative wind stress curl pattern associated with the wind jet spins up a cyclonic eddy north of the wind jet axis and an anticyclonic eddy to the south and that the strength of the dipole is proportional to the strength of the wind jet. The wind jet exhibits significant interannual variability, which is reflected in the strength of the dipole. The dipole can persist for several months after the wind jet disappears and can have cross-basin surface currents up to 1 m/s. The dipole structure observed in SLA during August 2001 was confirmed with in situ current observations made with an ADCP, which also showed that the dipole currents extended to 100–200 m (see also Sofianos and Johns 2007). The Tokar Dipolar eddy is not typically evident in the various OGCM simulations because the wind fields used to force the models do not adequately resolve the narrow Tokar Wind Jet.

Unlike the Tokar Dipolar eddy, several of the other eddies identified by Quadfasel and Baudner (1993) and others do show up consistently in most OGCM simulations, although with varying intensity and spatial scale. Prime among these are the apparently persistent anticyclonic eddy centered near 23°N and the cyclonic circulation in the far northern Red Sea (Clifford et al. 1997; Sofianos and Johns 2003; Biton et al.

2008). Sofianos and Johns (2003) suggested that generation of these eddies does not require cross-basin winds, or any wind forcing for that matter, and that some eddies form when buoyancy forcing alone is applied. They employed the Miami Isopycnic Coordinate Ocean Model (MICOM), first forced with both climatological winds and thermohaline fluxes and then with the two forcing mechanisms separately. <Query ID="Q3" Text="Please check whether the usage of the terms "thermohaline forcing-only" and "thermohaline-only forcing" are OK." ->The model mean surface circulation in the thermohaline-only forcing case was in general most similar to that with the full forcing, suggesting that the wind forcing plays a minor role, at least for the climatological mean surface circulation. For example, the cyclonic eddy usually observed at the northern end of the Red Sea was successfully reproduced in the thermohaline-only forcing case but had the opposite polarity in the wind-only forcing case. On the other hand, the 23°N anticyclonic eddy, clearly evident in their full-forcing model run, does not appear as a closed circulation cell in either of the separate forcing experiments, nor apparently in their sum. This example highlights the possible nonlinear interaction of the wind and thermohaline forcing and the overall complexity of the dynamics of the eddies in the Red Sea.

More support for the idea that at least some eddies in the Red Sea are not directly wind driven was presented by Chen et al. (2014), who used an unstructured grid, Finite-Volume Community Ocean Model (FVCOM) configured for the Red Sea and Gulf of Aden to investigate the dynamics of the eddy centered near 23°N (recent observations of this eddy are described in Chen et al. and in Sect. "Boundary Currents"). Horizontal model resolution varied from 3–8 km, and there were 30 layers in the vertical. Both high-resolution (from WRF) and lower-resolution (from NCEP) wind stress and buoyancy fluxes were used in separate numerical experiments to force the model. Through a series of model runs with different combinations of wind and buoyancy forcing, they found that the 23°N anticyclonic eddy was well reproduced compared to observations with heat flux forcing only, leading them to conclude that the eddy forms as a result of basin-scale (not local) geostrophic adjustment to the seasonal cycle in the large-scale buoyancy flux over several months. A southward coastal current on the western boundary seemed to play an important role in setting the eddy's strength. Wind forcing played a minor, but not insignificant role, affecting the intensity and vertical structure of the eddy.

Boundary Currents

In addition to the eddies discussed above, there is some evidence for near-surface currents that extend over hundreds of kilometers along the eastern and western boundaries of the Red Sea. These boundary currents extend over much

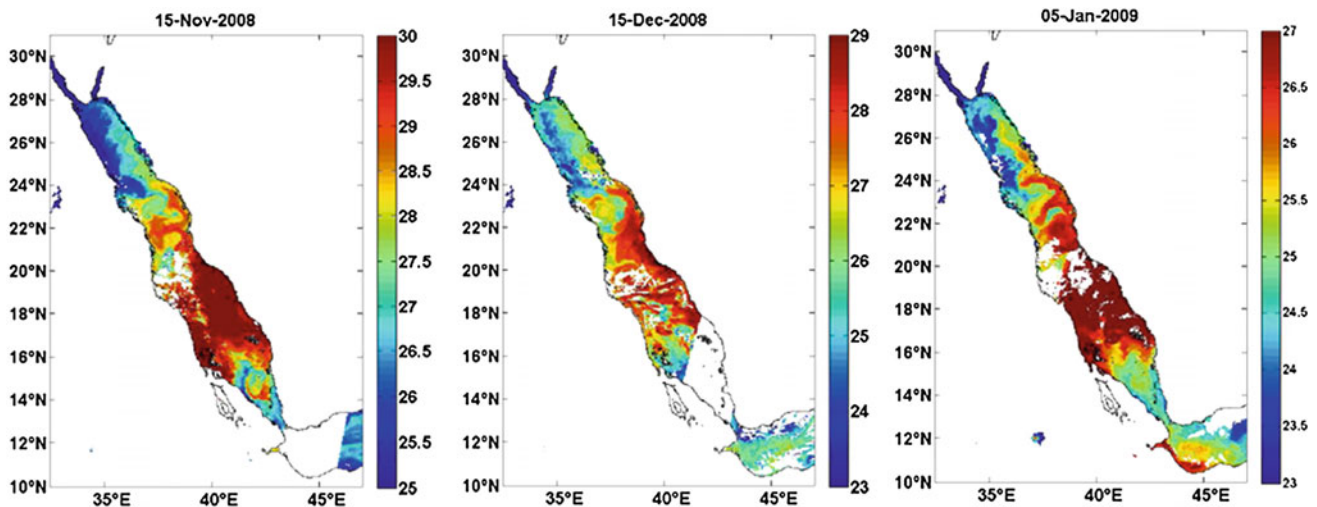


Fig. 6 Sea surface temperature imagery at three times during the winter of 2008–2009. The presence of a band of warm water along the eastern boundary of the northern half of the Red Sea suggests the presence of a northward-flowing boundary current carrying warm water

from the south to the north. This boundary current has been seen in numerical simulations of the Red Sea circulation, but there has been only limited observational evidence for its existence

larger spatial scales than the eddies. Until recently, indications of boundary currents were confined almost entirely to results from numerical model studies. For example, the climatological mean winter circulation in the MICOM model configuration used by Sofianos and Johns (2003) has a northward western boundary current in the southern Red Sea that crosses to the eastern boundary at about 16°N and continues to the northern end of the basin as a narrow eastern boundary current. This model boundary current system transports relatively warm, low-salinity surface water entering the Red Sea through Bab-al-Mandab northward as it is cooled and made more saline by air–sea fluxes. In the model, the water returns southward in a subsurface layer that eventually exits the Red Sea as a high-salinity, dense overflow (Murray and Johns 1997). A similar pattern of surface boundary currents was found in the climatological winter model results of Biton et al. (2010) and Yao et al. (2014b).

Invoking some theoretical ideas of McCreary et al. (1986) on the dynamics of eastern boundary currents, Sofianos and Johns (2003) argued that north of some critical latitude, traditional western intensification by westward-propagating Rossby waves is prevented because the Rossby wave group velocity is weaker than the mean eastward geostrophic flow induced by the meridional gradient in surface density. This critical latitude hypothetically sets the crossover latitude of the boundary current system from the western to eastern boundary. In another numerical study using the MIT GCM, Eshel and Naik (1997) obtained a similar pattern of western and eastern boundary currents, although the crossover

latitude of the western boundary current was much farther north (about 25°N) and was attributed to the collision of the northward western boundary current and the southward return flow of the eastern boundary current.

Sea surface temperature (SST) imagery from satellites supports the existence of an eastern boundary current in the northern half of the Red Sea resembling the one seen in the model simulations of Sofianos and Johns (2003). For example, Fig. 6 shows a sequence of infrared SST images taken from the Moderate Resolution Imaging Spectroradiometer (MODIS) instrument on NASA’s Aqua satellite during the winter of 2008–2009. A narrow band of warm water is visible along the eastern boundary of the northern half of the Red Sea, suggesting the presence of a northward-flowing boundary current carrying warm water from the south to the north. Although the thin band of warm water is nearly continuous, it is very convoluted, with meanders that extend across the full width of the Red Sea (e.g., near 21°N on 15 November) and significant temporal variability.

Further confirmation of these and other boundary currents, and their seasonal variability, has been delayed by a lack of in situ observations near the Red Sea boundaries. One exception is the recent observation during a joint WHOI–KAUST hydrographic survey in September–October 2011 of a narrow, subsurface current in the southern Red Sea transporting relatively cold, low-salinity, high-nutrient Gulf of Aden Intermediate Water (GAIW) northward along the eastern boundary in the southern Red Sea (Churchill et al. 2015).

The jet originates in the subsurface inflow of GAIW through Bab-al-Mandab during the summer (Southwest) monsoon (Murray and Johns 1997; Sofianos et al. 2002), and its anomalous properties had previously been observed in the Red Sea as far north as about 19°N (Smeed 1997; Sofianos and Johns 2007). The recent observations, the first comprehensive ones near the eastern boundary north of 17°N, reveal that GAIW was being carried in a coherent subsurface jet at depths of 50–100 m with maximum speed of 0.3 m/s. Some of the boundary current transport apparently was turning eastward into deep channels on the Farasan Banks, but there is evidence in hydrographic properties that GAIW also extended along the eastern boundary of the Red Sea to at least 24°N (see also Sect. 'Boundary Currents'). GAIW was also being advected into the basin interior by a large-scale anticyclonic eddy. The subsurface jet transporting GAIW along the eastern boundary was recently successfully simulated in the modeling study of Red Sea summer circulation using the MIT GCM by Yao et al. (2014a). The pathways of GAIW through the Red Sea, which is the only oceanic supply of new nutrients (Souvermezoglou et al. 1989), likely have significant implications for the spatial and temporal distributions of primary production (Churchill et al. 2015).

Recent Observations in the Eastern Red Sea

In 2010 and 2011, WHOI and KAUST conducted two hydrographic and current surveys of the eastern Red Sea. Until that time, what was known about the basin-scale eastern Red Sea circulation north of 17°N came entirely from numerical model simulations (Clifford et al. 1997; Eshel and Naik 1997; Sofianos and Johns 2003). These models suggested the presence of numerous cyclonic and anticyclonic eddies, as well as boundary currents with different seasonal patterns. The main purpose of the WHOI–KAUST hydrographic surveys was to provide modern seasonal snapshots of the sea surface-to-sea floor distribution of currents and water properties for comparison with remote sensing measurements and numerical model simulations. Here, we focus on the upper-layer circulation and hydrography (temperature, salinity, and density) based on the in situ observations collected during these surveys.

The first survey was carried out from March 16 to 29, 2010, on the *R/V Aegaeo* and covered the eastern half of the Red Sea north of 22°N. A total of 111 full-depth conductivity–temperature–depth (CTD) profiles were obtained during the cruise, mainly along nine cross-slope transects, with an average station spacing of 10 km along the transects

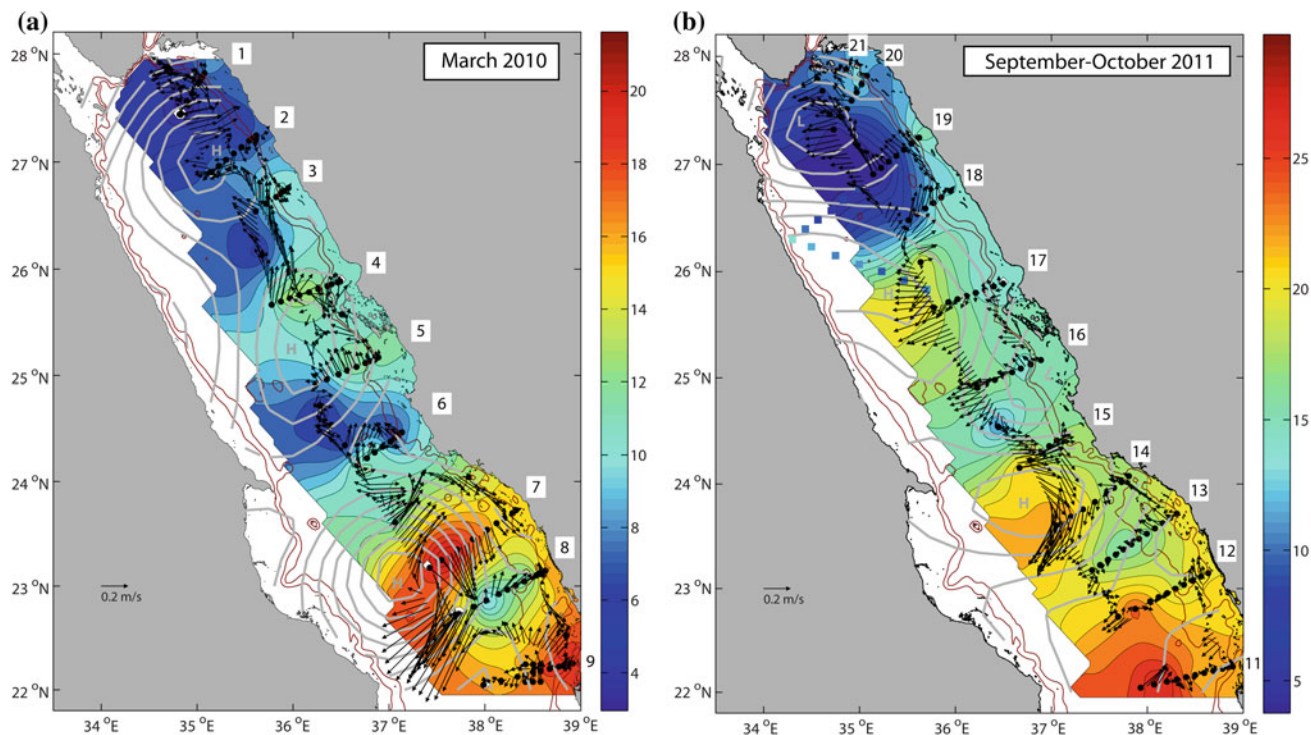


Fig. 7 a and b ADCP velocity vectors averaged horizontally in 5 km distance bins along the cruise track and vertically over the top 200 m during (a) March 2010 and (b) September–October 2011 survey cruises. Color shading indicates 10–200 dbar geopotential anomaly ($\times 10$ to display in dynamic cm). Colored squares in (b) also indicate

dynamic height but for select CTD stations occupied during August 2001 (Sofianos and Johns 2007). Gray contours show average SLA for the 2-week period of the 2010 and 2011 in situ measurements, contoured every 2 cm. The 200 and 500 m bathymetric contours from ETOPO2 are also indicated with magenta lines

(Fig. 7a). The cruise began in Thuwal, Saudi Arabia, transited northward to transect 1, then worked the transects 1–9 southward and ended in Thuwal. Heavy winds during transect 1 interrupted the cruise while the vessel took shelter in the lee of an island near the entrance to the Gulf of Aqaba. These transects plus several more, numbered 11–22, were occupied again (from south to north) during the second half of the second survey, which took place from September 27, 2011 to October 10, 2011, on the same vessel (Fig. 7b). Transects 1–10 in 2011 were occupied in the southern Red Sea—here we focus only on the area common to both surveys, 22–28°N. A vessel-mounted ADCP provided continuous measurements of current speed and direction from 18 m down to about 600 m depth along the entire cruise track at a vertical resolution of 8 m during both cruises.

The average vertical profiles of current speed from the ADCP measurements during the two cruises (not shown) indicate a surface-intensified vertical structure with average surface values of 0.24–0.27 m/s and 600 m speeds of 0.06–0.07 m/s. On average, 75–95 % of the vertical shear occurred over the top 200 m of the water column. Therefore, to summarize the upper ocean density field and currents, Fig. 7 shows the geopotential anomaly at 10 m relative to 200 m at each CTD station (multiplied by 10 to express as dynamic height in dynamic cm) and ADCP velocity vectors averaged over the same vertical scale. The strongest circulation feature

in the 2010 survey was an anticyclonic eddy centered near 23°N, with maximum 0–200 m average speed of 0.6 m/s. This is the same feature found in nearly all OGCM simulations and was identified by Quadfasel and Baudner (1993) as one of the more persistent eddies in the Red Sea. The circulation sense observed with the ADCP is consistent (assuming geostrophic balance to lowest order) with the slope of dynamic height on transects 7 and 8 (increasing offshore). The eddy also is clearly evident in the distribution of sea level anomaly, with a 10–12 cm sea level maximum elevation along transect 7 (Fig. 7a, gray contours). The 10 to 200 m dynamic height difference across the flank of the eddy was less, only 6–7 dynamic cm on CTD transects 7 and 8, but neither transect unambiguously reached the eddy center, where dynamic height would reach its maximum value. Furthermore, the eddy currents measured with the ADCP extended to nearly 400 m; the 10 to 400 m dynamic height (not shown) increased offshore by 12 dynamic cm along transect 7, quantitatively similar to the SLA.

Volume transport across transect 7 in the top 200 m estimated from ADCP velocities was -5.4 Sv (southward). This is an order of magnitude larger than the transport associated with the vertical overturning circulation, whose annual mean value is estimated from direct current observations in the strait to be about 0.4 Sv (Murray and Johns 1997; Sofianos et al. 2002). It is also larger than eddy transport estimates made by

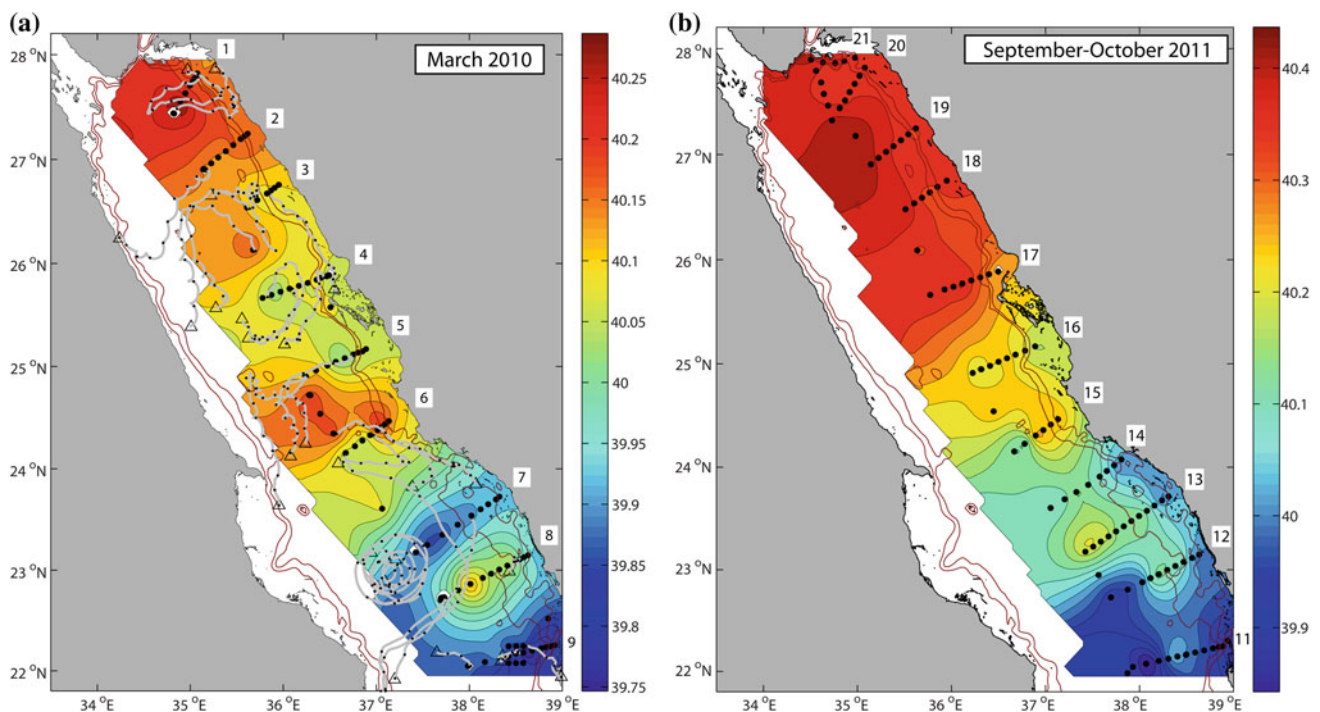


Fig. 8 a and b Vertically averaged (0–200 m) salinity (color shading) for the two survey cruises. Superimposed in (a) are the trajectories of 28 Davis-type surface drifters released during the 2010 cruise, only

from the launch position to the end of March, with *small dots* shown once daily along the tracks

Quadfasel and Baudner (1993) using a 400 m level of no motion in their geostrophic velocity calculations. The tracks of three surface drifters released near the anticyclonic eddy center (Fig. 8a) confirm its closed circulation. One drifter circulated in the eddy for 138 days and had a mean looping radius and speed of 27 km and 0.34 m/s, respectively, and a mean looping period of 6.6 days.

There is no evidence of a continuous northward eastern boundary current during the March 2010 cruise, such as seen in the climatological mean winter simulation of Sofianos and Johns (2003) and inferred from the early winter SST images in Fig. 6. Rather a complex pattern of eddies and boundary current segments was observed. Dynamic height shows a slight increase (about 4–5 dynamic cm) toward the eastern boundary on transects 8 and 9 due to relatively fresher and warmer water in the upper 200 m within 30 km of the boundary (Figs. 8a and 9a), accompanied by a weak northward flow component. However, currents on transect 7 were southward right up to the eastern boundary, interrupting any possible continuous northward-flowing eastern boundary current. Such a boundary current, if it exists, may have been obscured by the more energetic eddy field in March 2010 (as suggested in model results from Yao et al. 2014b) or may be in the process of dying out after the peak in buoyancy forcing that occurs earlier in the winter (Fig. 8).

Farther north, ADCP velocities and dynamic height gradients are generally weaker and indicate a circulation pattern of eddies and/or meanders. On several transects, dynamic height was higher adjacent to the eastern boundary (and northward currents were measured with ADCP), resulting from warmer and fresher water near the boundary compared to offshore stations (e.g., transects 1, 3 and 5). Transports (10–200 m) across these transects were northward 1.8 Sv (5), 0.2 Sv (3), and 0.6 Sv (1). Drifter tracks and velocity vectors suggest a closed cyclonic circulation in the far northern Red Sea in the vicinity of transect 1. On transects 2 and 4, as on transect 7, lowest salinity and highest temperature were found offshore of rather than against the eastern boundary (Figs. 8a and 9a), and all observations indicate anticyclonic circulation with southward flow near the eastern boundary. In both cases, the SLA fields also indicate a local maximum (anticyclone), although the patterns of SLA and dynamic height/velocity do not line up as closely with each other as they did for the anticyclonic eddy near 23°N.

Of particular note is the southward drift of surface drifters west of the CTD transects. After low-pass filtering to remove inertial oscillations, typical southward speeds of these drifters were 0.2–0.3 m/s, with occasional higher values up to 0.5–0.6 m/s (see also Chen et al. 2014). The trajectories show little evidence of eddies and/or meanders in the

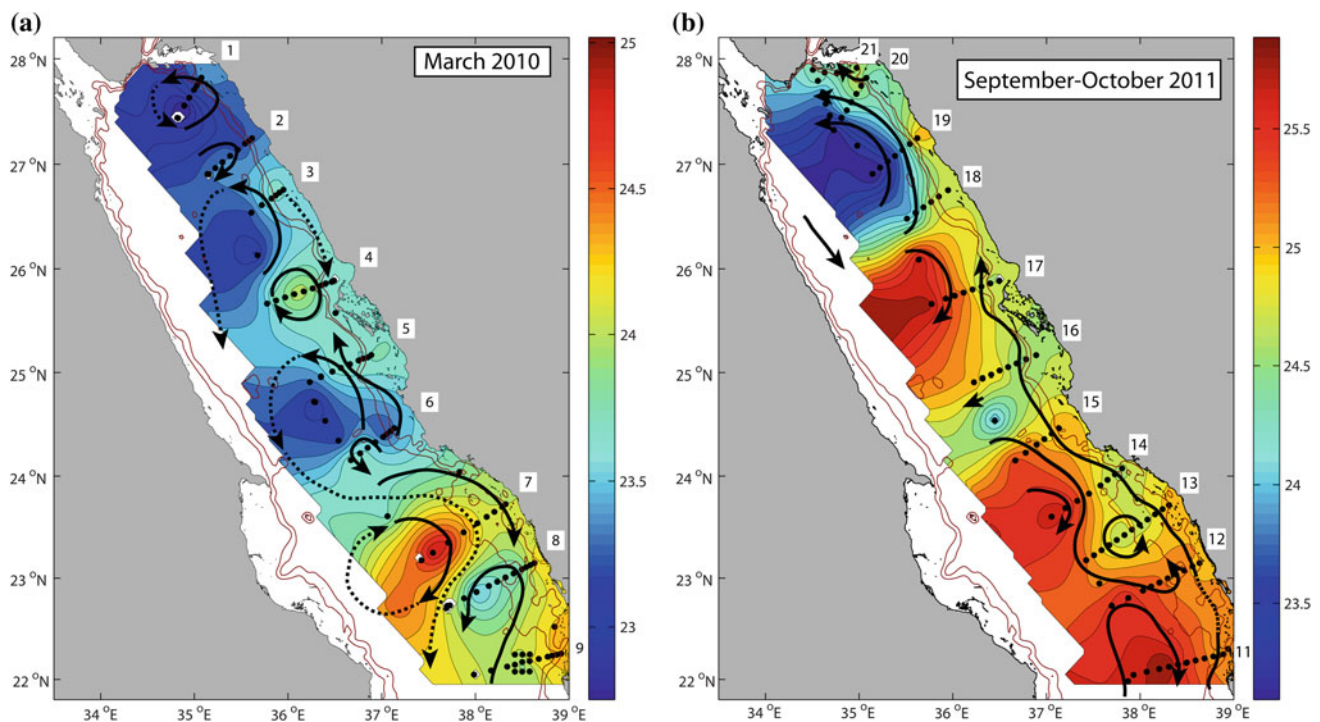


Fig. 9 a and b Schematic diagrams illustrating major circulation features during the two survey cruises, superimposed on the 0–200 m vertically averaged potential temperature (*color shading*). *Solid lines* are based on ADCP velocities and surface drifters (where the

trajectories are consistent with ADCP vectors). *Dotted lines* indicate features only observed in drifters. Bathymetric contours are 200 and 500 m

western region until they reach the vicinity of the anticyclonic eddy centered near 23°N, when some of these southward-moving drifters were deflected eastward then southward around the perimeter of the anticyclonic eddy there. Chen et al. (2014) successfully captured this southward flow near the western boundary and its continuation around the 23°N eddy based on the trajectories of particles initialized in the northern region of their numerical simulations.

Figure 9a summarizes the circulation in the northeastern Red Sea during the March 2010 hydrographic survey. The strongest currents in the region were associated with several 100–200 km diameter anticyclonic eddies centered near 27°N, 25.5°N, and 23°N, with the 23°N anticyclonic eddy being the strongest. The eddies were separated by areas of cyclonic flow. Salinity generally increased northward and westward; minimum 0–200 m average salinity (39.75) was observed at the southern limit of the survey area, while the maximum (40.29) was observed in the interior northern region. Far from a simple monotonically increasing meridional structure, salinity was lower (and temperature was higher) in anticyclonic eddies compared to cyclonic ones. Although not fully resolved by these observations confined to the eastern Red Sea, the circulation pattern is suggestive of a meandering northward transport of relatively warm, low-salinity water near the eastern boundary, with offshore meanders forming eddies of similarly fresher water. On the other hand, the eddy at 23°N appears to have completely blocked (at least temporarily) any northward penetration of warmer, fresher water from the south, based on the wrapping of southward-moving surface drifters around its eastern flank. The eddy's location and strength may be seasonally modulated and not always pressed up against the eastern boundary (see below and Chen et al. 2014). Surface drifters provide strong evidence of persistent southward flow in the western part of the northern Red Sea. On the largest spatial scale, there is qualitative consistency between the in situ observations and the sea level anomaly field, with three anticyclonic features in the surface circulation, which roughly correspond to three regions of anticyclonic flow in the in situ observations. The best match in both location and amplitude is for the 23°N eddy. Not surprisingly, the in situ observations reveal smaller-scale currents that cannot be resolved by altimetry.

In the September–October 2011 survey, strong eddy-like circulation features were again present (Fig. 7b). Maximum 10–200 m average speeds were about 0.4 m/s, similar to those reported by Sofianos and Johns (2007) along an axial ADCP transect in August 2001. The strongest currents line up approximately with high and low SLA features, especially the cyclonic circulation centered near 27°N and the anticyclonic eddy near 24°N. Sea level and dynamic height anomalies are similar for these features: about 5 cm (24°N

eddy) and 4 cm (27°N). Transports across transects 18, 19, 20, and 22 were 1.2, 1.8, 1.7, and 1.8 Sv, respectively, indicating a more vigorous and larger meridional scale cyclonic circulation in the northern region during this survey compared to the March 2010 survey, consistent with the model results of Sofianos and Johns (2003) and Biton et al. (2008).

Farther south, there was a slight increase in dynamic height (typically not more than a few dynamic cm) within about 30 km of the eastern boundary on transects 11–17. This is consistent with the directly measured velocities, which indicate a narrow, possibly continuous, band of northward flow. In some transects, the northward coastal flow is separated from offshore current features by a minimum in the middle of the transects (12–17). Salinity and temperature observations indicate that this coastal current transported relatively low-salinity, cold water (compared to offshore water) northward (Figs. 8b and 9b). This is likely indicative of a northward extension of GAIW, which enters the Red Sea as an intermediate layer (30–100 m) through Bab-al-Mandab during the summer months (Murray and Johns 1997; Smeed 1997; Sofianos et al. 2002; Sofianos and Johns 2007). Churchill et al. (2015) report on the GAIW distribution all along the eastern boundary of the Red Sea based on the full 2011 hydrographic survey data. Northward 0–200 m, along-slope transport in this boundary current (measured from the minimum transport in the middle of each transect) ranged from 1.0 Sv across transect 13 to 0.1 Sv across transect 15 and 0.2 Sv across transect 17. Vertical sections of velocity indicate that this northward boundary current has a subsurface maximum (see Churchill et al. 2015). From transect 18 northward, there was still northward along-slope flow across the transects, and the lowest salinities were found near the boundary, but the northward flow was not intensified against the eastern boundary as in transects farther south. The water near the boundary was warmer relative to the significantly colder water in the interior. The cold, high-salinity interior in the northern region produces a pool of minimum in dynamic height and relatively strong cross-basin velocities (~ 0.4 m/s) between transects 17 and 18. The western half of the cyclonic circulation was unfortunately not observed during the 2011 survey (no drifters). However, Sofianos and Johns (2007) observed southward flow in two transects near the western boundary in 2001.

Salinity averaged in the upper 200 m increased northward along the eastern boundary; the minimum was 39.83 on transect 11 and 40.37 on transect 20. Maximum salinity in the survey area was 40.44 in the cold, high-salinity pool centered near 27°N. Note that near-surface salinities were everywhere higher than in March 2010. This seems surprising at first given that the net freshwater flux to the atmosphere reaches an annual minimum during summer (Fig. 4; see also Sofianos and Johns 2002). Plots of salinity

versus density for 2010 and 2011 in the northern Red Sea (not shown) reveal that salinity is higher in 2011 on all isopycnals down to at least 200 m. This suggests that the higher summer values are not solely the result of shoaling of isopycnals in the cyclonic interior of the northern Red Sea during summer. Rather, these results point to the importance of advection of fresher water into the region from the south during winter. Without more hydrographic observations like these, it is impossible to determine how interannual variability in the supply of fresher water to the northern Red Sea may impact salinity distributions. As summarized in Fig. 9b, the strongest currents in 2011 were associated with the anticyclonic circulation near 24°N and the cyclonic cell centered near 27°N. ADCP velocities and T-S measurements indicate a possibly continuous northward along-slope eastern boundary current transporting relatively cold, low-salinity water as far north as about 25.5°N. Low-salinity water was also found against the boundary north of that latitude, but a boundary-intensified current was not distinguishable from the generally northward flow associated with the offshore area of low dynamic height. While the strongest eddies correspond moderately well in location and amplitude with the SLA, the narrow eastern boundary current, with its dynamic height amplitude of at most a few dynamic cm over ~30 km, is not resolvable from altimetry.

Given the moderately good agreement between dynamic height and SLA for the basin-scale circulation features away from the boundaries, it is of interest here to use the nearly 20-year time series of SLA to investigate how the observed circulation features fit into the seasonal cycle of cyclonic and

anticyclonic eddy circulations. This is illustrated in Fig. 10, which shows a Hovmoller diagram of the mean seasonal cycle of relative vorticity along the central axis of the northern Red Sea, calculated from the gradients in SLA. Positive (negative) relative vorticity corresponds to cyclonic (anticyclonic) circulation. The midpoints of the 2010 and 2011 surveys are indicated by vertical dashed lines. During March, the climatological mean vorticity shows an AC centered at about 23°N that is close to a climatological maximum amplitude at the time of year of the March 2010 survey. As pointed out earlier, this feature in the Hovmoller diagram corresponds well to the AC observed during the March 2010 cruise (Fig. 9a). Based on the climatology, this AC near 23°N apparently spins up quickly beginning in early December, reaches an initial maximum in March, translates northward to about 24°N, reaches a second peak in amplitude in mid-August, then spins down by the end of October.

The timing of the AC spin-up in early December is consistent with the arrival of relatively warm, low-salinity Gulf of Aden Surface Water, which begins to enter the Red Sea through Bab-al-Mandab in early September (Sofianos et al. 2002) (~1100 km to the south) assuming a mean northward advection rate of about 0.15 m/s. These results suggest, but do not confirm, that the 23°N AC eddy may spin up in this region every year as a result of the arrival of northward-flowing Gulf of Aden Surface Water interacting somehow with the local bathymetry and/or other eddies.

Immediately north of this AC, the vorticity climatology indicates near-zero vorticity at the time of year of the March 2010 survey, but just before the cruise period, a strong

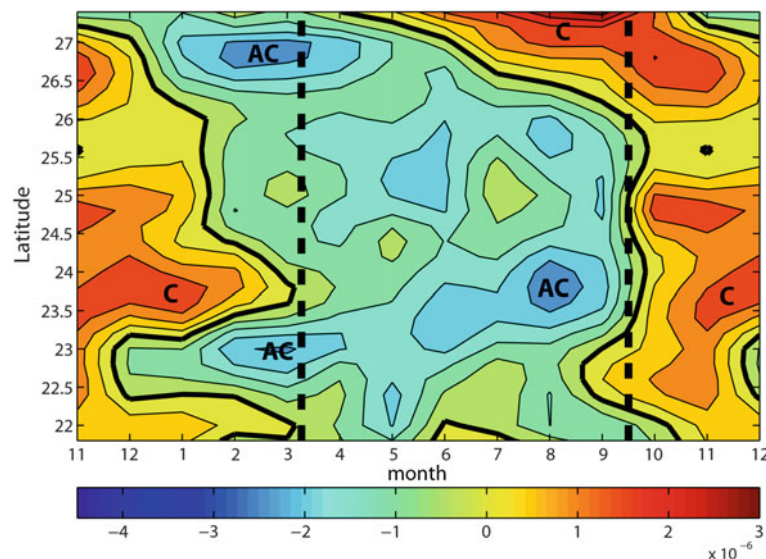


Fig. 10 Hovmoller diagram of annual mean relative vorticity along the Red Sea axis as a function of latitude and month of the year (marked at the midpoint of each month). Heavy dashed lines indicate the midpoint of each of the two hydrographic surveys. Negative relative vorticity

(blue) indicates anticyclonic (AC) circulation, and positive (red) represents cyclonic (C) circulation. Relative vorticity was estimated from surface geostrophic velocity calculated from AVISO sea level anomaly maps

cyclonic eddy is evident in the climatology. The remnants of such a cyclonic eddy might be what are seen in the March 2010 ADCP velocity observations, centered near 24°N (Fig. 7a). This cyclonic eddy reaches its climatological maximum amplitude during November to January. The September–October 2011 survey caught several circulation features that can also be related to features in the SLA climatology, including a string of AC, C, and AC eddies across transects 11–15.

At 27°N, anticyclonic vorticity dominates in the climatology from mid-December to June, after which it appears to migrate southward and be replaced in the northern basin by cyclonic vorticity, which itself migrates southward in December. This switch in polarity of the circulation in the northern Red Sea between winter and summer is consistent with what was observed in the 2010 and 2011 current surveys, with anticyclonic circulation seen in March 2010 (transect 2, Fig. 7a) and cyclonic circulation dominating in October 2011 (transects 18, 19, 20, and 22; Fig. 7b).

Summary and Conclusions

Recent direct estimates of air–sea fluxes from a moored meteorological buoy in the east-central Red Sea have exposed a new phenomenon that may be responsible for much of the heat and freshwater flux out of the basin during winter, namely cold, dry mountain-gap wind jets blowing westward off the coast of Saudi Arabia. These measurements have also revealed shortcomings in the climatological air–sea flux products often used to force numerical models.

Ocean numerical model studies and observations over the past several decades have revealed that the horizontal circulation of the Red Sea is energetic and complex, dominated by boundary currents and quasi-stationary eddies, both anticyclonic and cyclonic. Transports associated with the eddies, typically 1–5 Sv, are an order of magnitude larger than the annual mean overturning transport (~ 0.4 Sv). The cross-basin component of the wind stress has been shown to be important in spinning up at least one eddy pair, while other eddies are reproduced in numerical model simulations forced only with buoyancy fluxes. The eddy formation mechanism in the latter case is still unclear. Satellite altimetry is reasonably successful in capturing the largest, most energetic eddies in the interior of the basin, but not the narrow (<50 km width) boundary currents. The nearly 20-year time series of altimetric measurements also reveals an annual cycle in the average location and strength of eddies, including the persistent 23°N eddy and the reversal in the northern circulation cell. The persistence of eddies at particular latitude bands is most likely due to the interaction of the buoyancy-driven circulation with capes and promontories in the bathymetry, although in at least one case eddy

latitude is fixed by the location of an intense summer cross-basin wind jet. New observations near the eastern boundary north of 17°N point toward a greater northward extension of GAIW during late summer than previously reported, although it is significantly diluted by exchange with the interior and with coral reef channels along its path. While there is renewed interest for making new in situ observations of air–sea fluxes, currents, and hydrographic properties in the Red Sea, there remains a strong need for sustained, basin-scale measurements to thoroughly evaluate numerical models and to increase our understanding of the roles of wind and buoyancy forcing in driving Red Sea circulation and its variability on seasonal and longer time scales. Specifically, time series of currents and water properties near both boundaries, transects across the full width of the basin, and air–sea flux measurements at several latitudes are needed to validate numerical simulations and test ideas about the dynamics governing Red Sea circulation.

Acknowledgments Data collection during the WHOI-KAUST collaboration was made possible by Award Nos. USA00001, USA00002, and KSA00011 to the WHOI by the KAUST in the Kingdom of Saudi Arabia.

References

- Acker J, Leptoukh G, Shen S, Zhu T, Kempler S (2008) Remotely-sensed chlorophyll *a* observations of the northern Red Sea indicate seasonal variability and influence of coastal reefs. *J Mar Syst* 69:191–204
- Biton E, Gildor H, Peltier WR (2008) Red sea during the last glacial maximum: implications for sea level reconstruction. *Paleoceanography* 23(1). doi:10.1029/2007pa001431
- Biton E, Gildor H, Trommer G, Siccha M, Kucera M, van der Meer MTJ, Schouten S (2010) Sensitivity of Red Sea circulation to monsoonal variability during the holocene: an integrated data and modeling study. *Paleoceanography* 25. doi:10.1029/2009pa001876
- Chen C, Ruixiang L, Pratt L, Limeburner R, Beardsley R, Bower AS, Jiang H, Abualnaja Y, Liu X, Xu Q, Lin H, Lan J, Kim T-W (2014) Process modeling studies of physical mechanisms of the formation of an anticyclonic eddy in the central Red Sea. *J Geophys Res Oceans* 119. doi:10.1002/2013JC009351
- Churchill JA, Bower A, McCorkle DC, Abualnaja Y (2015) The transport of nutrient-rich Indian Ocean water through the Red Sea and into coastal reef systems. *J Mar Res* (in press)
- Clifford M, Horton C, Schmitz J, Kantha LH (1997) An oceanographic nowcast/forecast system for the Red Sea. *J Geophys Res* 102:25101–25122
- Eshel G, Naik N (1997) Climatological coast jet collision, intermediate water formation, and the general circulation of the Red Sea. *J Phys Oceanogr* 27(7):1233–1257
- Fairall CW, Bradley EF, Hare JE, Grachev AA, Edson JB (2003) Bulk parameterization of air–sea fluxes: Updates and verification for the COARE algorithm. *J Clim* 16:571–591
- Farrar JT, Lentz S, Churchill J, Bouchard P, Smith J, Kemp J, Lord J, Allsup G, Hosom D (2009) King Abdullah University of Science and Technology (KAUST) mooring deployment cruise and field-work report, technical report. Woods Hole Oceanographic Institute, Woods Hole, Mass, 88 pp

- Hickey B, Goudie AS (2007) The use of TOMS and MODIS to identify dust storm source areas: the Tokar delta (Sudan) and the Seistan basin (south west Asia). In: Goudie AS, Kalvoda J (eds) *Geomorphological Variations*. P3K, Prague, pp 37–57
- Jiang H, Farrar JT, Beardsley RC, Chen R, Chen C (2009) Zonal surface wind jets across the Red Sea due to mountain gap forcing along both sides of the Red Sea. *Geophys Res Lett* 36, L19605
- Josey S, Kent E, Taylor P (1999) New insights into the ocean heat budget closure problem from analysis of the SOC air–sea flux climatology. *J Clim* 12:2856–2880
- Maillard C (1971) Etude hydrologique et dynamique de la Mer Rouge en hiver. *Annales de l'Institut océanographique*, Paris 49(2):113–140
- McCreary JP, Shetye SR, Kundu PK (1986) Thermohaline forcing of eastern boundary currents: with application to the circulation off the west coast of Australia. *J Mar Res* 44:71–92
- Morcos SA (1970) Physical and chemical oceanography of the Red Sea. *Oceanogr Mar Biol Annu Rev* 8:73–202
- Morcos S, Soliman GF (1972) Circulation and deep water formation in the northern Red Sea in winter. UNESCO, *L'Océanographie Physique de la Mer Rouge*, pp 91–103
- Murray SP, Johns W (1997) Direct observations of seasonal exchange through the Bab el Mandeb Strait. *Geophys Res Lett* 24(21):2557–2560
- Naval Oceanography Command Detachment (1993) U.S. Navy regional climatic study of the Red Sea and adjacent waters. NAVAIR 50-1C-562. National Oceanic and Atmospheric Administration, Asheville
- Papadopoulos VP, Abualnaja Y, Josey SA, Bower A, Raitos DE, Kontoyiannis H, Hoteit I (2013) Atmospheric forcing of the winter air–sea heat fluxes over the northern Red Sea. *J Clim* 26:1685–1701
- Patzert WC (1974) Wind-induced reversal in Red Sea circulation. *Deep Sea Res* 21:109–121
- Pedgley DE (1974) An outline of the weather and climate of the Red Sea. *L'Océanographie Physique de la Mer Rouge*. United National Educational, Scientific, and Cultural Organization, Paris, pp 9–27
- Phillips OM (1966) On turbulent convection currents and the circulation of the Red Sea. *Deep Sea Res* 13(6):1149–1160
- Quadfasel D, Baudner H (1993) Gyre-scale circulation cells in the Red Sea. *Oceanol Acta* 16:221–229
- Raitos DE, Pradhan Y, Brewin RJW, Stenichikov G, Hoteit I (2013) Remote sensing the phytoplankton seasonal succession of the Red Sea. *PLoS ONE* 8(6):64909
- Raitos DE, Hoteit I, Prihartato PK, Chronis T, Triantafyllou G, Abualnaja Y (2011) Abrupt warming of the Red Sea. *Geophys Res Lett* 38(14), L14601. doi:[10.1029/2011GL047984](https://doi.org/10.1029/2011GL047984)
- Risien CM, Chelton DB (2008) A global climatology of surface wind and wind stress fields from eight years of QuikSCAT scatterometer data. *J Phys Oceanogr* 38:2379–2413
- Smeed D (1997) Seasonal variation of the flow in the Strait of Bab al Mandab. *Oceanol Acta* 20(6):773–781
- Sofianos SS, Johns WE (2002) An Oceanic General Circulation Model (OGCM) investigation of the Red Sea circulation: 1. Exchange between the Red Sea and the Indian Ocean. *J Geophys Res* 107 (C11):3196
- Sofianos SS, Johns WE (2003) An Oceanic General Circulation Model (OGCM) investigation of the Red Sea circulation: 2. Three dimensional circulation in the Red Sea. *J Geophys Res* 108 (C3):3066
- Sofianos SS, Johns WE (2007) Observations of the summer Red Sea circulation. *J Geophys Res* 112:C06025
- Sofianos SS, Johns WE, Murray SP (2002) Heat and freshwater budgets in the Red Sea from direct observations at Bab el Mandeb. *Deep Sea Res Part II* 49:1323–1340
- Souvermezoglou E, Metzl N, Poisson A (1989) Red Sea budgets of salinity, nutrients, and carbon calculated in the Strait of Bab el Mandab during the summer and winter season. *J Mar Res* 47:441–456
- Tragou E, Garrett C (1997) The shallow thermohaline circulation of the Red Sea. *Deep-Sea Res* 44:1355–1376
- Tragou E, Garrett C, Outerbridge R, Gilman G (1999) The heat and freshwater budgets of the Red Sea. *J Phys Oceanogr* 29:2504–2522
- Yao F, Hoteit I, Pratt L, Bower A, Zhai P, Köhl A, Gopalakrishnan G, Rivas D (2014a) Seasonal overturning in the Red Sea: part 1. Model verification and summer circulation. *J Geophys Res* 119:2238–2262. doi:[10.1002/2013JC009331](https://doi.org/10.1002/2013JC009331)
- Yao F, Hoteit I, Pratt L, Bower A, Zhai P, Köhl A, Gopalakrishnan G, Rivas D (2014b) Seasonal overturning in the Red Sea: part 2. Winter circulation. *J Geophys Res* 119:2263–2289. doi:[10.1002/2013JC009331](https://doi.org/10.1002/2013JC009331)
- Yu L, Weller RA (2007) Objectively analyzed air–sea heat fluxes for the global ice-free oceans (1981–2005). *Bull Am Meteorol Soc* 88:527–539
- Zhai P, Bower A (2013) The response of the Red Sea to a strong wind jet near the Tokar Gap in summer. *J Geophys Res* 118(1):421–434
- Zhang Y, Rossow WB, Lacis AA, Oinas V, Mishchenko MI (2004) Calculation of radiative fluxes from the surface to top of atmosphere based on ISCCP and other global data sets: refinements of the radiative transfer model and the input data. *J Geophys Res* 109: D19105. doi:[10.1029/2003JD004457](https://doi.org/10.1029/2003JD004457)